A Partial Domain Approach to Enable Aortic Flow Simulation Without Turbulent Modeling

Taha S. Koltukluoglu[1,⋆], Christian Binter[3], Christine Tanner[1], Sven Hirsch[2], Sebastian Kozerke[3], Gábor Székely[1], and Aymen Laadhari[1]

[1] Computer Vision Lab., Swiss Federal Institute of Technology, Zürich, Switzerland
ktaha@vision.ee.ethz.ch
[2] Inst. of Applied Simulation, Zurich University of Applied Sciences, Wädenswil, Switzerland
[3] Inst. for Biomed. Eng., Swiss Federal Institute of Technology, Zürich, Switzerland

Abstract. Analysis of hemodynamics shows great potential to provide indications for the risk of cardiac malformations and is essential for diagnostic purposes in clinical applications. Computational fluid dynamics (CFD) has been established as a valuable tool for the detailed characterization of volumetric blood flow and its effects on the arterial wall. However, studies concentrating on the aortic root have to take the turbulent nature of the flow into account while no satisfactory solution for such simulations exists today. In this paper we propose to combine magnetic resonance imaging (MRI) flow acquisitions, providing excellent data in the turbulent regions while showing only limited reliability in the boundary layer, with CFD simulations which can be used to extrapolate the measured data towards the vessel wall. The solution relies on a partial domain approach, restricting the simulations to the laminar flow domain while using MRI measurements as additional boundary conditions to drive the numerical simulation. In this preliminary work we demonstrate the feasibility of the method on flow phantom measurements while comparing actually measured and simulated flow fields under straight and spiral flow regimes.

1 Introduction

A wide range of flow problems can be approximated using computer assisted numerical methods. The physics of the flow field is described by the Navier-Stokes equations in terms of non-linear partial differential equations. Usually an analytical solution does not exist (except for simple geometries). Therefore, the governing equations are discretized resulting in an algebraic system of equations. Simplifications can be applied depending on, e.g., the compressibility and/or viscosity of the fluid. In biomechanical studies, the blood flow is usually approximated with a divergence-free assumption in large arteries.

⋆ This work was supported by the Swiss National Science Foundation grant 320030-149567.

N. Navab et al. (Eds.): MICCAI 2015, Part II, LNCS 9350, pp. 544–551, 2015.
DOI: 10.1007/978-3-319-24571-3_65

Analysis of hemodynamics shows great potential to provide indications for the risk of cardiac malformations and is essential for diagnostic purposes in clinical applications [4]. In the last decade, combined studies based on computational fluid dynamics and magnetic resonance imaging have been under extensive research. Recent advances in three-directional velocity encoded phase contrast MRI [2] enable to capture complex flow patterns within the arteries including the aortic root. Some major drawbacks of MRI are the limitations with respect to signal-to-noise ratio, resolution and partial volume effects, which restrict the analysis of hemodynamic parameters [3].

Inflow velocity data are frequently determined by 2-D flow MRI and used in CFD as boundary conditions (BCs) [5]. Morbiducci et al. [6] recently demonstrated the importance of realistic inflow conditions and its substantial impact on the flow field. In [8], flow rates were applied as BCs. In [7], Boutsianis implemented a Schwarz-Christoffel technique to map measured MRI data for setting BCs at an inflow surface.

All of these studies apply the flow conditions at the inlet and perform flow simulations on the entire domain. However, due to the complex geometry of the aortic root and high flow velocities at positions near the valves, turbulent flow can be observed in a core region of the ascending aorta. In the surrounding the flow is transitional i.e., depending on the heart phase, it usually oscillates between laminar and turbulent [10]. Still in all cases, the velocities are zero at the vessel wall due to adhesion forces. Since blood is a viscid fluid, a parabolic profile is developed very near the vascular wall, which is lined by a laminar boundary layer. These regions are illustrated in Fig. 1b.

Numerical simulation of turbulent flows is a notoriously complex problem and no satisfactory solution for turbulent blood flow simulation exists today. Under these circumstances it is mandatory to search for alternative approaches when investigating the physiology of the aortic root. While MRI phase contrast flow measurements provide excellent data in the turbulent region, no reliable measurements can be expected in the boundary layer due to very poor signal-to-noise ratio at low velocities.

In this paper we propose a new method which explores this complementarity between CFD simulations and MRI measurements by restricting the simulation to a partial domain covering regions with laminar flow, while using MRI measurements at positions with sufficiently high velocities as additional BCs to drive the numerical simulations. The approach has been tested by comparing MRI measurements on a rigid vessel phantom with preliminary simulation results using both classical CFD and partial domain simulations.

2 The Partial Domain Approach

Let us define a set of manifolds $\Gamma_i, \Gamma_p, \Gamma_o, \Gamma_w \subset \mathbb{R}^3$. The subscripts stand for inlet, partial layer, outlet and wall, respectively. We define a domain $\Omega \subset \mathbb{R}^3$ with the boundary $\partial\Omega = \Gamma_i \cup \Gamma_p \cup \Gamma_o \cup \Gamma_w$ (see Fig. 1a and 1b). The flow is modeled as homogeneous, incompressible and Newtonian fluid governed by the

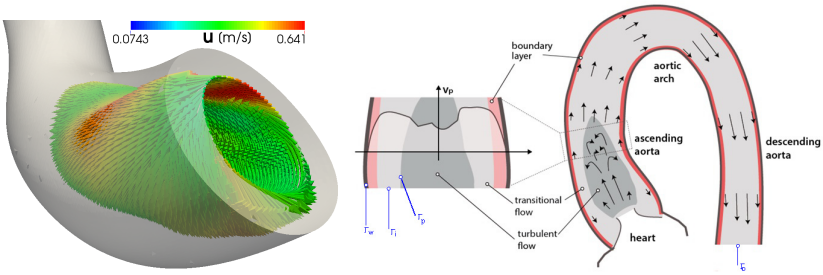

Fig. 1. (a): Partial domain, (b): Illustration of laminar boundary layer, transitional region and turbulent region.

Navier Stokes equations (2.1) and (2.2). Let $\boldsymbol{u} = \boldsymbol{u}(t, \boldsymbol{x}) : [0, T] \times \Omega \to \mathbb{R}^3$ be the velocity and $p = p(t, \boldsymbol{x}) : [0, T] \times \Omega \to \mathbb{R}$ stands for the pressure, $t \in [0, T]$ being the time and $\boldsymbol{x} \in \Omega$. Suitable initial and BCs of both types (Dirichlet and Neumann) are required to ensure the well-posedness of the problem, which reads: $\forall t \in [0, T]$, find $\boldsymbol{u}$ and p such that

$$\rho\left(\partial_t \boldsymbol{u} + \boldsymbol{u} \cdot \nabla \boldsymbol{u}\right) - \mu \Delta \boldsymbol{u} + \nabla p = f \qquad \text{in } [0, T] \times \Omega \tag{2.1}$$

$$\nabla \cdot \boldsymbol{u} = 0 \qquad \text{in } [0, T] \times \Omega \tag{2.2}$$

$$\boldsymbol{u}(0, \cdot) = \tilde{\boldsymbol{u}}^{\star}(\cdot) \qquad \text{in } \{0\} \times \Omega \tag{2.3}$$

$$\boldsymbol{u} = \boldsymbol{0} \quad \text{and} \quad \nabla p \cdot \boldsymbol{n} = 0 \qquad \text{on } [0, T] \times \Gamma_w \tag{2.4}$$

$$\boldsymbol{u} = \boldsymbol{s} \quad \text{and} \quad \nabla p \cdot \boldsymbol{n} = 0 \qquad \text{on } [0, T] \times (\Gamma_i \cup \Gamma_p) \tag{2.5}$$

$$p = 0 \quad \text{and} \quad \nabla \boldsymbol{u} \cdot \boldsymbol{n} = \boldsymbol{0} \qquad \text{on } [0, T] \times \Gamma_o \tag{2.6}$$

where ρ is the density, μ is the viscosity, $\boldsymbol{n}$ is the outward normal of the corresponding boundary and $\tilde{\boldsymbol{u}}^{\star}$ is some observation (see Section 4). The body forces are neglected in this work. The equations (2.1) and (2.2) are the momentum and conservation equations, respectively. Non-homogeneous BCs are applied on the inlet and the partial layer for $\boldsymbol{u}$ (2.5). The rest of the applied BCs are homogeneous. By restricting the simulations to the aortic volume between the surface Γ_p and the wall, we have to account only for regions with laminar flow and rely on standard numerical methods for solving the Navier-Stokes equations. The price we have to pay for it is, that additional BCs have to be defined on the surface Γ_p. In what follows, the computed velocities are denoted as $\boldsymbol{u}_c$.

When performing dynamic simulations, the temporal resolution of MRI measurement is not sufficient. Due to the noisy MRI velocities, strict interpolation schemes enforcing precise agreement with the observed data are not appropriate to generate denser sampling and we rely on an approximation approach by defining a function $s : [0, T] \times (\Gamma_i \cup \Gamma_p) \to \mathbb{R}^3$ (2.5), whose components are spline regression model functions used to prescribe the observed velocity components,

$\tilde{\boldsymbol{u}}^{\star}$, on $\Gamma_i \cup \Gamma_p$. The defined model functions are cubic splines of class C^2 with uniformly distributed nodes. To obtain the model coefficients, the penalized regression spline method (2.7) was applied to minimize the sum of squares fitting error and (weighted by λ) the parameter irregularity. This was used as the interpolation function for the BCs on the inlet and partial layer (2.5). For each space position in $\Gamma_i \cup \Gamma_p$, the interpolation in time reads

$$\forall t \in [0,T], \quad \boldsymbol{s}(t) = \arg\min_{\mathbf{a}} \left(\sum_k |\tilde{\boldsymbol{u}}^{\star}(t^k) - \mathbf{a}(t^k)|^2 + \lambda \int |\mathbf{a}''(\tau)|^2 d\tau \right) \tag{2.7}$$

3 Experimental Setup

In-vitro experiments were performed on a 3-D print of a rigid replica realistically mimicking the geometry of the human aortic root, ascending aorta, the arch without its branches and descending aorta (see Fig. 2a). A centrifugal pump (of 3.9 bar maximum pressure) was connected to the aorta and an open circuit was created by connecting the inlet and outlet tubes to a reservoir. The flow rates were controlled through a ball bearing valve. Linear phase correction were applied to compensate for the background phase induced by Eddy-current. The scans were performed with a 3T Philips scanner using a 6-element cardiac coil.

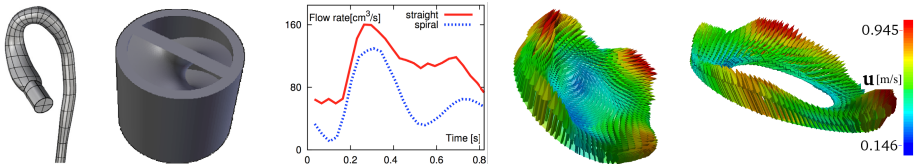

Fig. 2. (a): Rigid phantom, (b): 3-D printed screw to create the spiral motion, (c): Flow rates $[cm^3/s]$ for straight and spiral cases, (d and e): Spiral flow pattern visualized at inlet of full and partial domain at peak systole.

Measurements were taken with straight and spiral motion patterns. In order to generate the spiral motion as shown in Fig. 2d and 2e, a small 3-D printed device was additionally placed at the inlet, forcing the incoming fluid to develop a helical flow (see Fig. 2b). The acquisition parameters for straight flow were TR/TE: 5.63/3.25 ms, flip angle: 10^o, VENC: 150 cm/s, FOV: $[160 \times 260 \times 50]$ mm^3, acquired voxel size: $[1.25 \times 1.25 \times 1.25]$ mm^3, temporal resolution: 28.0 ms. The parameters for spiral flow were TR/TE: 4.87/2.99 ms, flip angle: 10^o, VENC: 100 cm/s, FOV: $[160 \times 320 \times 50]$ mm^3, acquired voxel size: $[2 \times 2.08 \times 2]$ mm^3, temporal resolution: 34.16 ms. As a working fluid, a mixture of H_2O and carboxymethyl cellulose (CMC) was used to increase the viscosity of water. To ensure laminar flow, the viscosity of the mixture was increased to the range of blood viscosity in the aorta. Fig. 2c shows the acquired flow rates in cm^3/s.

4 Preprocessing

Reconstructed MR images provide anatomical and three-directional flow data. The aortic geometry was segmented using snake evolution method in ITK-SNAP (www.itksnap.org) and smoothed using the VMTK framework (www.vmtk.org). In addition, a high resolution surface description was available from the model's 3-D print. This was rigidly registered to each segmentation using the ITK point-set to point-set registration method (www.itk.org). A hexahedral mesh was generated within the high resolution surface using OpenFOAM's snappyHexMesh and transfered to each segmentation using the registration result.

A general outlier detection scheme [1] initially applied to particle image velocimetry data, was implemented to detect spurious velocity vectors of the MRI. The method is based on normalization of the usual median test respecting the local fluctuations of the velocity field. The applicability of the normalized median test has been verified by Westerweel and Scarano [1] for a large variety of flow conditions with Reynolds numbers ranging from 10^{-1} to 10^{7}.

The detected outliers have to be replaced by some values such as from linear interpolation. However, thereby the divergence-free property of the flow field most probably gets lost. We therefore apply Helmholtz-Hodge decomposition [11]. The space of square integrable functions can be decomposed into divergence-free, curl-free and gradient of harmonic components as in (4.1) and (4.2). Let $\bar{\boldsymbol{u}}_{\mathrm{MRI}}$ be the projection of already denoised MRI flow data on Ω. The orthogonal space splitting states $\bar{\boldsymbol{u}}_{\mathrm{MRI}} = \tilde{\boldsymbol{u}} + \boldsymbol{u}_{\wedge} + \boldsymbol{u}^{\star}$. Hence, the divergence free component can be extracted from $\tilde{\boldsymbol{u}}^{\star} = \tilde{\boldsymbol{u}} + \boldsymbol{u}^{\star} = \bar{\boldsymbol{u}}_{\mathrm{MRI}} - \boldsymbol{u}_{\wedge}$, which reads as $\mathscr{P}_{\perp}$ (4.3).

The data were first linearly interpolated onto the computational domain and the decomposition was applied thereafter for each available heart phase. The applied Helmholtz-Hodge decomposition recovers the divergence-free property of the flow field to a great extent (Fig. 3). In [9], the feasibility of the decomposition was validated for a steady state. This is extended to a dynamic case under pulsatile flow conditions to enable robust comparisons between CFD and MRI.

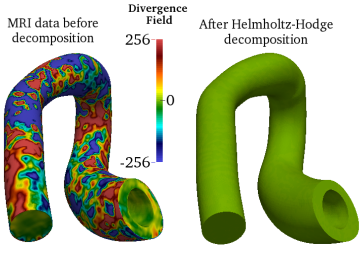

Fig. 3. Systolic divergence fields.

$$\left(L^2(\Omega)\right)^3 = \mathrm{H}_{\mathrm{div},0}(\Omega) \oplus \mathrm{H}_{\mathrm{curl},0}(\Omega) \oplus \mathrm{H}_{\mathrm{har}}(\Omega) \tag{4.1}$$

$$\begin{aligned} \mathrm{H}_{\mathrm{div},0}(\Omega) &= \Big\{ \tilde{\boldsymbol{u}} \in (L^2(\Omega))^3 : \ \boldsymbol{u} \cdot \boldsymbol{n}|_{\partial\Omega} = 0, \\ &\qquad \nabla \cdot \tilde{\boldsymbol{u}} \in L^2(\Omega), \nabla \cdot \tilde{\boldsymbol{u}} = 0 \Big\} \\ \mathrm{H}_{\mathrm{curl},0}(\Omega) &= \Big\{ \boldsymbol{u}_{\wedge} = \nabla q : \ q \in H_0^1(\Omega) \Big\} \\ \mathrm{H}_{\mathrm{har}}(\Omega) &= \Big\{ \boldsymbol{u}^{\star} = \nabla h : \ h \in H^1(\Omega), \ \Delta h = 0 \Big\} \end{aligned} \tag{4.2}$$

$$\begin{aligned} &\mathscr{P}_{\perp} : \ \textit{find } \tilde{\boldsymbol{u}}^{\star} = \bar{\boldsymbol{u}}_{\mathrm{MRI}} - \nabla q, \ \textit{such that}: \\ &\Delta q = \nabla \cdot \bar{\boldsymbol{u}}_{\mathrm{MRI}} \text{ in } \Omega \\ &q = 0 \text{ on } \Gamma_w \quad \text{and} \quad \nabla q \cdot \boldsymbol{n} = 0 \text{ on } \partial\Omega \backslash \Gamma_w \end{aligned} \tag{4.3}$$

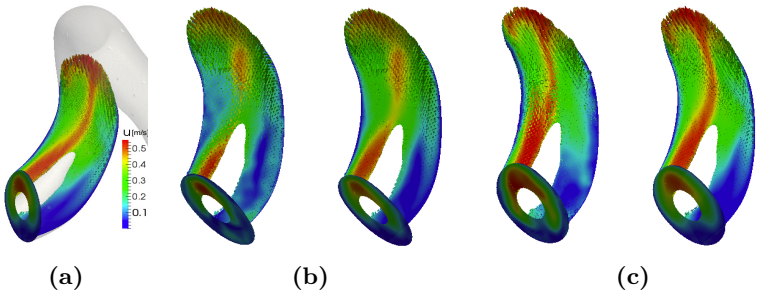

Fig. 4. Illustration of (a): cross-sectional partial domain, (b/c): mid/peak systole for measured (b/c left) and computed (b/c right) velocities.

5 Results

We tested the ability of the partial domain approach to reproduce MRI measurements in the selected domain similarly well as the traditional CFD method on the full domain of the aortic lumen. For this, we performed simulations with both methods and compared them with the MRI data acquired under straight flow conditions. Flow patterns were first qualitatively compared by visual inspection. Fig. 4 illustrates mid and peak systole on a cross-sectional slice of the data with straight flow generated by partial domain simulation. The left most Fig. 4a shows the position of a slice cut at the aortic root for further investigation. The orientation of the slice was chosen to cover both the partial domain and the flow domain immediately thereafter. In Fig. 4b and 4c, flow patterns of measured velocities are illustrated on the left side and the computed velocities on the right side of each sub-figure with respect to peak (Fig. 4c) and mid systole (Fig. 4b), respectively. It can be seen that the pattern is reasonably similar between the left and right plots of each sub-figure.

In order to confirm these qualitative observations, the simulation results of the velocities, $\boldsymbol{u}_c$, have been quantitatively compared to the divergence-free projection of the MRI measurements, $\tilde{\boldsymbol{u}}^\star$. The comparisons consist of root mean square error (nRMSE) normalized against the maximum velocity of the measurements (5.1). Furthermore, we evaluate the flow direction error (FDE) and the relative velocity magnitude error (rVME) defined in (5.2). The FDE delivers a dimensionless value between 0 (same direction) and 2 (opposite directions). These error measurements are less accurate near the wall boundaries in comparison to the middle of the lumen due to segmentation and registration errors. In addition, the phantom material delivers almost no relevant signal (i.e. mainly noise) at and near the boundaries, but noise. Respecting these uncertainties, the errors were also evaluated on a contracted domain within the lumen at a distance d (in mm) away from the aortic surface. We will refer to these errors as nRMSE_d, FDE_d and rVME_d, respectively. In addition, defining $\boldsymbol{x} \in \Omega$, we introduce the characteristic function $\chi_d(\boldsymbol{x})$, which is equal to 1 if the position $\boldsymbol{x}$ is more than

d apart from the nearest surface point, and 0 otherwise. Furthermore, we define $\Omega_d = \{\boldsymbol{x} \in \Omega : \chi_d(\boldsymbol{x}) = 1\}$, V_d its volume and T is the time of one cardiac cycle.

$$\mathrm{nRMSE}_d = \left(\frac{100}{\max\limits_{t,\Omega_d} |\tilde{\boldsymbol{u}}^\star|} \right) \sqrt{\frac{1}{V_d \cdot T} \int_t \int_{\Omega_d} |\tilde{\boldsymbol{u}}^\star - \boldsymbol{u}_c|^2} \tag{5.1}$$

$$\mathrm{FDE}_d(t) = \sqrt{\int_{\Omega_d} \left(1 - \frac{\tilde{\boldsymbol{u}}^\star \cdot \boldsymbol{u}_c}{|\tilde{\boldsymbol{u}}^\star||\boldsymbol{u}_c|} \right)^2 \frac{1}{V_d}} \quad \mathrm{rVME}_d(t) = \sqrt{\int_{\Omega_d} \frac{|\tilde{\boldsymbol{u}}^\star - \boldsymbol{u}_c|^2}{|\tilde{\boldsymbol{u}}^\star|^2 V_d}} \tag{5.2}$$

Table 1. Dimensionless flow direction errors (FDE_d) and relative velocity magnitude errors (rVME_d) for full domain (Full) and partial domain (Part) cases measured at peak systole and early diastole phase within the whole ($d = 0$ mm) and contracted ($d = 2$ mm) volume (Ω_d).

Straight flow		Systole		Diastole	
		FDE_d	rVME_d	FDE_d	rVME_d
Full	$d = 0$	0.27	0.48	0.28	0.70
Part	$d = 0$	0.26	0.45	0.27	0.68
Full	$d = 2$	0.19	0.35	0.24	0.48
Part	$d = 2$	0.18	0.33	0.21	0.49

Spiral flow		Systole		Diastole	
		FDE_d	rVME_d	FDE_d	rVME_d
Full	$d = 0$	0.12	0.47	0.17	0.55
Part	$d = 0$	0.12	0.47	0.18	0.60
Full	$d = 2$	0.14	0.45	0.06	0.38
Part	$d = 2$	0.08	0.41	0.07	0.41

We evaluated the errors for the entire lumen ($d = 0$ mm) and for the contracted domain by $d = 2$ mm. The evaluations were performed on the peak systole and end diastole over both the partial and the full domain. Furthermore, to assess the performance over the pulsation for one cardiac cycle, we evaluated the time integrated errors nRMSE_d for $d = 0$ and $d = 2$ mm. All simulations were performed using $\approx$ 95.000 cell volumes. To perform a consistency check and mesh analysis, the straight flow with partial domain case was also simulated with a much finer mesh, using $\approx$ 600.000 cell volumes.

For straight flow, the results presented on Table 1 (left) show very similar deviations between measured and calculated flow for most measures. The time integrated nRMSE_d errors were for $d = 0$, 13.62% and 15.60%, and for $d = 2$, 12.73% and 13.19% for full and partial domains, respectively. Furthermore, the partial domain case with the finer mesh resulted in $\mathrm{nRMSE}_0 = 14.82\%$ and $\mathrm{nRMSE}_2 = 12.92\%$. This suggests that partial domain simulations can well replace full domain calculation which cannot be performed under turbulent flow conditions. Note that, it could be more appropriate to consider the errors for $d = 2$, as MRI flow measurements are unreliable near to the boundary. In order to investigate the dependency of this observation on the complexity of the flow field, we performed the same comparison using the spiral flow measurements. The results for FDE and rVME are listed in Table 1 (right). In addition, nRMSE_2 were 16.34% for full domain and 18.83% for partial domain, respectively.

6 Discussion and Conclusion

A novel approach based on partial domains has been proposed for vascular flow simulations. The velocity measurements were projected onto the computational domain by linear interpolation and Helmholtz-Hodge decomposition was applied to recover the divergence-free property of the flow field. The simulation results were compared against the decomposed field both qualitatively and quantitatively. The work is still in an early stage and we have presented preliminary results. The centrifugal pump cannot capture the backflow, hence does not fully reflect the pulsating nature of blood flow. In-vitro MRI experiments under straight and spiral motion patterns with pulsatile flow showed the feasibility of the application. The partial domain approach reveals a great potential to investigate hemodynamics related parameters near the wall regions of tubular structures.

References

1. Westerweel, J., Scarano, F.: Universal outlier detection for PIV data. Exp. Fluids 39, 1096–1100 (2005)
2. Markl, M., Frydrychowicz, A., Kozerke, S., Hope, M., Wieben, O.: 4D flow MRI. Magn. Reson. Im. 36, 1015–1036 (2012)
3. Stankovic, Z., Allen, B.D., Garcia, J., Jarvis, K.B., Markl, M.: 4D flow imaging with MRI. Cardio. Diag. and Thera. 4(2), 173–192 (2014)
4. Katritsis, D., Kaiktsis, L., Chaniotis, A., Pantos, J., Efstathopoulos, E.P., Marmarelis, V.: Wall shear stress: theoretical considerations and methods of measurement. Prog. Cardiovasc. Dis. 49(5), 307–329 (2007)
5. Leuprecht, A., Kozerke, S., Boesiger, P., Perktold, K.: Blood flow in the human ascending aorta: a combined MRI and CFD study. J. of Eng. Maths. 47(3-4), 387–404 (2003)
6. Morbiducci, U., Ponzini, R., Gallo, D., Bignardi, C., Rizzo, G.: Inflow boundary conditions for image-based computational hemodynamics: Impact of idealized versus measured velocity profiles in the human aorta. J. of Biomech. 46(1), 102–109 (2013)
7. Gupta, S., Boomsma, K., Poulikakos, D., Boutsianis, E.: Boundary Conditions by Schwarz-Christoffel Mapping in Anatomically Accurate Hemodynamics. Ann. of Biomed. Eng. 36(12), 2068–2084 (2008)
8. Steinman, D.A., Milner, J.S., Norley, C.J., Lownie, S.P., Holdsworth, D.W.: Image-Based Computational Simulation of Flow Dynamics in a Giant Intracranial Aneurysm. American J. of Neurorad. 24, 559–566 (2003)
9. Koltukluoglu, T.S., Hirsch, S., Binter, C., Kozerke, S., Székely, G., Laadhari, A.: A Robust Comparison Approach of Velocity Data Between MRI and CFD Based on Divergence-Free Space Projection. In: Intern. Symp. on Biomed. Imag. (2015)
10. Stein, P.D., Sabbah, H.N.: Turbulent Blood Flow in the Ascending Aorta of Humans with Normal and Diseased Aortic Valves. Cir. Res. 39, 58–65 (1976)
11. Denaro, F.M.: On the application of the Helmholtz-Hodge decomposition in projection methods for incompressible flows with general boundary conditions. Int. J. Numer. Meth. Fluids 46, 43–69 (2003)